Activatable Small-Molecule Photoacoustic Probes that Cross the Blood–Brain Barrier for Visualization of Copper(II) in Mice with Alzheimer's Disease

Shichao Wang, Zonghai Sheng,* Zhenguo Yang, Dehong Hu, Xiaojing Long, Gang Feng, Yubin Liu, Zhen Yuan, Jingjing Zhang, Hairong Zheng, and Xuanjun Zhang*

Abstract: *Copper enrichment in the brain is highly related to Alzheimer's disease (AD) pathogenesis, but in vivo tracing of Cu^{2+} in the brain by imaging techniques is still a great challenge. In this work, we developed a series of activatable photoacoustic (PA) probes with low molecular weights (less than 438 Da), **RPS1–RPS4**, which can specifically chelate with Cu^{2+} to form radicals with turn-on PA signals in the near-infrared (NIR) region. Introducing the electron-donating group N,N-dimethylaniline into the probe was found to significantly enhance the radical stability and PA intensity. The best probe in the series, **RPS1**, showed a fast response (within seconds) to Cu^{2+} with high selectivity and a low PA detection limit of 90.9 nM. Owing to the low molecular weight and amphiphilic structure, **RPS1** could effectively cross the blood–brain barrier (BBB) and thus allowed us, for the first time, to visualize Cu^{2+} in vivo via PA imaging in the brains of AD mice.*

Copper is the third-most abundant trace metal in the human body and plays a vital role in physiological and pathological activity. Abnormal alterations in cellular copper homeostasis are connected to serious diseases, including cardiovascular disorders, Wilson disease, and Alzheimer's disease (AD).[1] Some studies have noted that Cu^{2+} enrichment in the brain has a close relationship with AD pathogenesis.[2] Redox-active Cu^{2+} in the brain was implicated in the generation of reactive oxygen species (ROS), leading to the high oxidative stress that is a proposed factor in accelerating the assembly and neurotoxicity of AD amyloid-β (Aβ) fibrils.[3] Therefore, highly sensitive imaging/detection of Cu^{2+} in the brain of patients suffering from AD is essential to comprehensively understand its pathological events in the brain. Currently, many fluorescent probes have been explored and applied to stain for Cu^{2+} in cells and living organisms with good performance.[4] However, in vivo fluorescence imaging of Cu^{2+} in the brain is still a great challenge due to limited penetration depth (approximately 1 mm), difficulty in crossing the blood–brain barrier (BBB), and the fluorescence quenching resulting from the paramagnetic effect of Cu^{2+}.[5]

Compared with fluorescence technology, photoacoustic (PA) imaging combines optical imaging and ultrasound imaging into a hybrid modality, exhibiting multiscale spatial resolution with deep tissue penetration (centimeter depths).[6] Because of these advantages, PA imaging with functional probes has been widely applied in biomedical imaging,[7] disease detection,[8] and biosensing.[9] However, only a limited number of small-molecule PA probes with activatable features for detecting metal ions have been reported.[9c,d, 10] Moreover, to the best of our knowledge, there has been no report of PA tracing for Cu^{2+} in the brain of animal models until now.
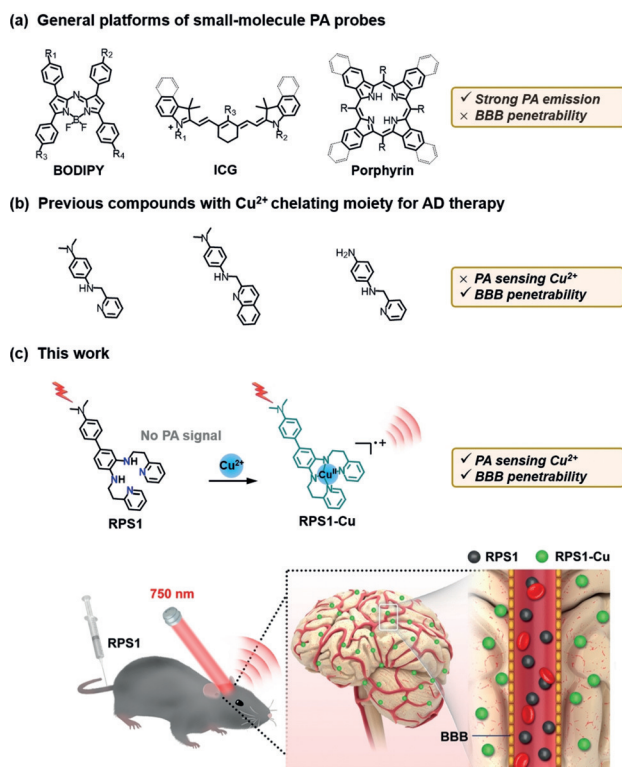
Theoretically, the design of small-molecule PA probes is mainly based on extending a large π-conjugated backbone, such as boron-dipyrromethene (BODIPY), indocyanine green (ICG), and porphyrin derivatives (Scheme 1a).[11] Even with strong PA emission, these probes generally have a large molecular mass that exceeds the threshold of 600 Da to cross the BBB.[12] Some of the compounds with a Cu^{2+} chelating moiety for AD therapy are able to cross BBB, but their insensitive absorption variation prevents their use as Cu^{2+} PA probes (Scheme 1b).[13] As unexplored PA contrast agents, aniline derivatives could form anilinyl radical complexes exhibiting near-infrared (NIR) absorption triggered by Cu^{2+}.[14] However, these complexes usually have a short lifetime in aqueous media because free radicals are able to abstract hydrogen from water.[15] In this work, inspired by the structures of AD drugs and aniline radicals, we designed a series of activatable PA probes, **RPS1–RPS4**, with a small molecular weight (less than 438 Da) and specific NIR PA detection of Cu^{2+}. To tune the PA intensity and water stability of the probes, we modified the molecular structure with electron-donating and electron-accepting groups. We found that the introduction of electron-donating groups, such as N,N-dimethylaniline (**RPS1**), led to an amplified PA emission in the NIR region and significantly improved the stability of the probes upon detecting Cu^{2+} in aqueous media. **RPS1** could effectively cross the BBB and thus allowed us for the first time the visualization of Cu^{2+} in vivo via PA imaging in AD mouse brains (Scheme 1c).

[*] Dr. S. Wang, G. Feng, Dr. Y. Liu, Prof. Z. Yuan, Prof. X. Zhang
Cancer Centre and Centre of Reproduction, Development and Aging,
Faculty of Health Sciences, University of Macau
Macau SAR (P. R. China)
E-mail: xuanjunzhang@um.edu.mo

Prof. Z. Sheng, Dr. D. Hu, X. Long, Prof. H. Zheng
Paul C. Lauterbur Research Center for Biomedical Imaging,
Institute of Biomedical and Health Engineering,
Shenzhen Institute of Advanced Technology,
Chinese Academy of Sciences, Shenzhen 518055 (P. R. China)
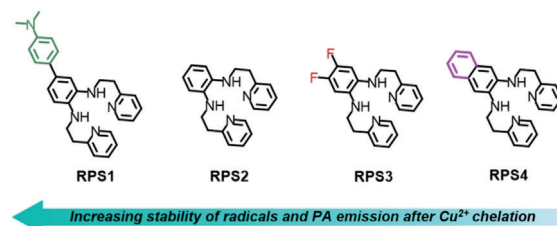E-mail: zh.sheng@siat.ac.cn

Z. Yang, Prof. J. Zhang
Affiliated Hospital of Guangdong Medical University
Zhanjiang 524001 (P. R. China)

Supporting information and the ORCID identification number(s) for the author(s) of this article can be found under:
https://doi.org/10.1002/anie.201904047.

Scheme 2. The structures of probes **RPS1**–**RPS4**.

complexes exhibited corresponding masses and high-intensity EPR signals, which indicated the existence of an unpaired electron and the formation of radicals.

For further imaging application, the stability of these radicals in aqueous media should be evaluated because the single electron has a strong proton-binding capacity and may abstract hydrogen from water molecules to quench the radical.[15] As shown in Figure S4a in the Supporting Information, the NIR absorption of **RPS4**–**Cu**, with a naphthalene structure, was quenched within 5 minutes. The double-fluorine substituents, with strong electron-accepting ability, decreased the lifetime of **RPS3**–**Cu** to about 1 hour. The absorbance of **RPS2**–**Cu** in water decreased substantially within 1 hour and then remained stable over the next few hours. Surprisingly, the introduction of *N,N*-dimethylaniline greatly increased the stability of **RPS1**-**Cu** to 30 hours, perhaps because the electron-donating group could stabilize the inert action of free radicals (Scheme 2 and Supporting Information, Table S1).

We tested the response of all probes to a variety of biologically relevant metal ions in PBS (pH 7.4, 0.02 M) and found that all **RPS1**–**RPS4** showed specific selectivity to Cu^{2+}, resulting in a unique NIR absorption (Supporting Information, Figures S5–S8). The competition experiment in the presence of mixed metal ions (Fe^{2+}, Fe^{3+}, Ni^{2+}, Co^{2+}, Cu^{2+}) also showed that **RPS1** with an electron-donating group had the most superior selectivity to Cu^{2+} (Supporting Information, Figure S9). A titration experiment was conducted on **RPS1** and **RPS2** by absorption spectra in PBS and fetal bovine serum (FBS), and the results demonstrated that the absorption spectra of both probes had a good linear fit with Cu^{2+} concentration. **RPS1** possessed a super low absorption limit of detection (7.2 nM), lower than **RPS2** (30.0 nM), and good stability in excess Cu^{2+} in PBS buffer (Figure 1c and Supporting Information, Figures S10 and S11).

Encouraged by the optimal features of **RPS1**, this probe was chosen as a potential activatable probe for subsequent PA imaging. To determine the optimal wavelength for PA imaging, the PA spectra of **RPS1** and its chelated complex were measured at wavelengths ranging from 680 to 970 nm using a Vevo LAZR imaging system.[16] As seen in Figure 1d, **RPS1** had no PA signal in this broad region. Upon chelation with Cu^{2+}, the **RPS1** complex possessed the strongest PA signal at approximately 710 nm, followed by dampening of the PA signal. PA selection contrast to Cu^{2+} of **RPS1** was overwhelmingly greater than that of other metal ions (Figure 1e). In PA quantitative analysis, the PA limit of detection was calculated to be as low as 90.9 nM (Figure 1f). This limit of detection was lower than the biological Cu^{2+} level and
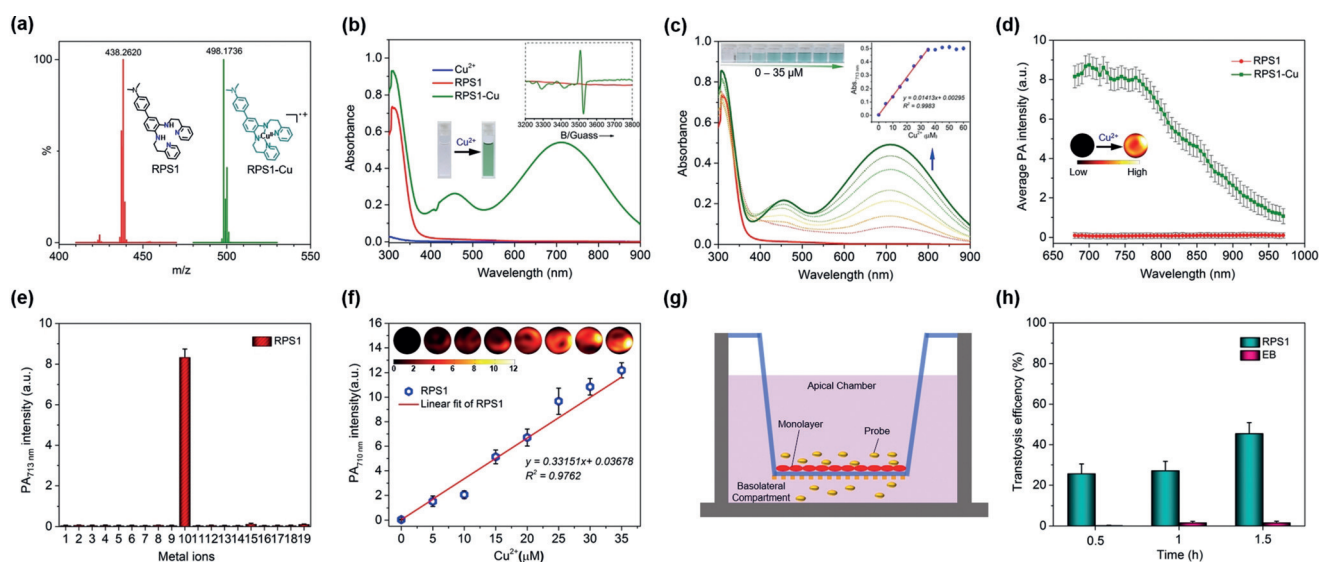

Scheme 1. Rational design of activatable PA probes for Cu^{2+} detection in AD mouse brain. a) General platforms of small-molecule PA probes. b) Previous compounds with Cu^{2+}-chelating moiety for AD therapy. c) The PA probe **RPS1** and a schematic diagram of **RPS1** crossing the blood–brain barrier (BBB) and detecting Cu^{2+}, as observed by PA imaging.

In PBS, all probe solutions exhibited a transparent color with absorption in the ultraviolet region. After the addition of Cu^{2+}, the color of the solution changed to green within seconds (Supporting Information, Movie 1). **RPS1**, with the electron-donating group *N,N*-dimethylaniline, exhibited the longest absorption wavelength (713 nm) and the strongest absorbance ($\varepsilon > 10\,000$) among the four probes in the presence of 1 equiv Cu^{2+} (Figure 1b and Supporting Information, Table S1). In contrast, the relatively weaker absorbance ($\varepsilon < 4100$) and blue-shifted absorption peak at approximately 690 nm for **RPS2**–**RPS4** metal-chelate complexes were attributed to the smaller conjugation systems and electron-acceptor groups (Supporting Information, Figure S1b). Upon addition of Cu^{2+}, **RPS1** had the strongest PA emission, which was at least approximately 2.5-times greater than that of the other probes at 700 nm excitation (Supporting Information, Figure S1c). In contrast to their lack of PA background signal, all probes displayed a substantial PA emission upon detecting Cu^{2+}, except **RPS4** because of the unstable free radical formed by the **RPS4**–**Cu** complex. To verify the formation of a π-radical monoanion in the chelated complexes that gave rise to the NIR absorption,[14a] we conducted mass spectrometry (MS) and electron paramagnetic resonance (EPR) spectroscopy of the free **RPS** probes and their chelated complexes (**RPS**–**Cu**) in solutions (Figure 1a, insert, Figure 1b and Supporting Information, Figures S2 and S3). The results show that all **RPS**–**Cu**

Figure 1. a) Mass spectra of **RPS1** and **RPS1**–**Cu**. b) The absorption spectra of **RPS1**, Cu^{2+}, and **RPS1**–**Cu** complex (all are 50 μM). The inset shows the EPR spectra of **RPS1** (2.5 mM) and **RPS1**–**Cu** in acetonitrile and PBS (v:v = 1:1) at room temperature. The color change of **RPS1** from transparent to deep green after addition of 1 equiv Cu^{2+}. c) Changes in the absorption spectra of **RPS1** (50 μM) after reaction with different concentrations of Cu^{2+} for 10 minutes. The inset shows the color of **RPS1** solution and calibration curve of the absorbance at 713 nm for the detection of Cu^{2+} in the range of 0–35 μM. d) PA spectra of 50 μM **RPS1** and **RPS1**–**Cu** from 680 to 970 nm. The inset shows the PA image of an **RPS1** and **RPS1**–**Cu** solution upon excitation at 710 nm. e) PA selectivity tests for **RPS1** (50 μM, 1) upon addition of metal ions (2: Li^+, 3: Na^+, 4: K^+, 5: Ca^{2+}, 6: Mg^{2+}, 7: Al^{3+}, 8: Fe^{2+}, 9: Fe^{3+}, 10: Cu^{2+}, 11: Zn^{2+}, 12: Ni^{2+}, 13: Mn^{2+}, 14: In^{3+}, 15: Co^{2+}, 16: Cd^{2+}, 17: Pb^{2+}, 18: Hg^{2+}, 19: Cu^+; 500 μM for Na^+, K^+, and Ca^{2+} and 50 μM for other metal ions) for 10 minutes. f) Calibration curve of the PA intensity at 710 nm for the detection for Cu^{2+} in the range of 0–35 μM. Above tests were performed in 0.02 M PBS solution at pH 7.4 unless otherwise specified. g) Schematic overview of the construction of an in vitro BBB model. h) The relative transcytosis amount of **RPS1** and **EB** in vitro within 1.5 hours. Experiments were repeated three times, and the data are presented as the mean ± SD (c, d, e, f, h).

indicated that **RPS1** has great potential for detecting Cu^{2+} in the brain by PA imaging.[4b]

The temperature stability of **RPS1**–**Cu** was monitored by absorption in PBS. As shown in Figure S12 in the Supporting Information, **RPS1**–**Cu** had no obvious absorption change in the range of 30 to 46 °C. Light irradiation of **RPS1** and **RPS1**–**Cu** for 3 hours indicated that both had good stability under ambient light (Supporting Information, Figure S13). **RPS1** was also selective for Cu^{2+} in the presence of ROS/reactive nitrogen species (RNS) and principally reductive biomolecules (ascorbic acid, methylglyoxal, glutathione, and cysteine, Supporting Information, Figure S14). At different pH values from 6.0 to 8.5, the **RPS1**–**Cu** complex also showed the desired stability (Supporting Information, Figure S15). In summary, these tests indicated that the free radical of the **RPS1**–**Cu** complex remained relatively inert toward possible in vivo surrounding factors. The binding affinity of **RPS1** for Cu^{2+} was evaluated as $1.18 \times 10^4 \, \text{M}^{-1}$ using the Benesi–Hildebrand method (Supporting Information, Figure S16), which was in the range of affinity of the second Cu^{2+} binding site of Aβ.[13] To confirm **RPS1** was able to detect Cu^{2+} in Aβ fibrillar aggregates, we applied **RPS1** to Cu–Aβ aggregates and found that it has a good linear response to Cu^{2+} in Aβ aggregates (Supporting Information, Figure S17).

Prior to in vivo PA imaging, the cytotoxicity of **RPS1** was examined in brain vascular endothelial (bEnd.3) cells using a viability assay (Supporting Information, Figure S18). The results showed that **RPS1** had negligible cytotoxicity toward bEnd.3 cells after incubation for 24 hours (probe concentration, 0–200 μM). The hemolytic analysis showed a low hemol-

ysis percentage (0.5 %) of red blood cells even at 40 μM **RPS1** (Supporting Information, Figure S19). The mouse blood panel parameters showed that the values of the three groups of mice presented slight or mild variations, which indicated that **RPS1** had the advantage of low in vivo cytotoxicity and adequate hemocompatibility (Supporting Information, Figure S20). Furthermore, hematoxylin and eosin (H&E) staining images of the major organs demonstrated that the probe-treated group had no distinct tissue damage compared to the control group (Supporting Information, Figure S21). The physiological stability of the probes in nude mice was evaluated by injecting a freshly prepared **RPS1**–**Cu** solution (100 μL at 50 μM) into the leg muscle. Following laser irradiation (750 nm), the PA signal of the injection site was detected (Supporting Information, Figure S22). PA imaging showed that the strong PA intensity of **RPS1-Cu** at the injection sites was much higher than that of the surrounding tissue, even after 200 minutes, indicating high in vivo stability.

To assess whether **RPS1** crosses the BBB, we measured the in vitro BBB-permeability efficacy of **RPS1** by transwell filters seeded with a bEnd.3 cellular monolayer according to a previously reported method.[17] The transwell model was separated into three typical spaces, i.e., the apical chamber, cellular monolayer, and basolateral compartment (Figure 1 g). The integrity of the cellular monolayer was monitored by transendothelial electrical resistance (TEER) and cell staining with crystal violet. As shown in Figure S23 in the Supporting Information, TEER reached a peak at about 7 days and the bEnd.3 cells densely seeded on the surface of

the filter. For the negative control group, Evans blue (**EB**), which has been widely used as a negative tracer to assess the permeability of endothelial-type barriers in normal brains without damage, was applied.[18] We chose **EB** as a negative control to ensure that the transwell model was reliable. After the addition of **EB** (10 μM) and **RPS1** (150 μM, very low toxicity to cells) into the apical chamber with a cellular monolayer, the absorbance of the solution on the basolateral side at 610 nm and 310 nm was measured three times every half hour. By calculating the absorbance based on Figure S24 in the Supporting Information, we found that **EB** was almost completely unable to cross the cell monolayer in the transwell model. In contrast, **RPS1** had good transport capability across the cell monolayer and reached an appreciable permeability efficiency of more than 40% after 1.5 hours (Figure 1h).

Based on the above favorable results of the photophysical and PA analysis, **RPS1** was applied to PA imaging to further confirm the feasibility of detecting Cu^{2+} in mouse brains. AD mice and age-matched normal mice were employed for comparison according previous reports.[19] In one group, AD and normal mice were all injected with **RPS1** (0.5 mg kg^{-1}) through tail-vein intravenous treatment. In another group, AD mice were injected with PBS as the control. As shown in Figure 2a, with the aid of ultrasound imaging, a whole map of the brains with distinct borders was obtained. For the brains of normal mice treated with **RPS1**, there was a weak PA signal, possibly due to the low amount of Cu^{2+} detection and endogenous hemoglobin in the brain blood vessels. The brains of AD mice showed widely distributed, strong PA signals throughout the whole cortex region. The AD mouse brains treated with PBS showed a weak PA signal mainly distributed over the narrow central area. The PA signal of PBS-treated AD mice has approximately the same intensity but a different distribution in the brain compared with probe-treated normal mice, which was possibly from the hemoglobin.

The mean PA intensity in the region of interest (ROI) of AD mice treated with the probe was 9.57-fold and 8.50-fold stronger than that of probe-treated normal mice and PBS-treated AD mice, respectively (Figure 2b). This result was in agreement with Cu^{2+} concentration ratio between AD and normal mice brain that was determined by inductively coupled plasma-atomic emission spectrometry (ICP-AES, Supporting Information, Table S2). Higher resolution and deeper ex vivo PA imaging of brains were performed using an advanced three-dimensional (3D) PA system. As shown in Figure S25 in the Supporting Information, the cerebral blood vessels (red ellipses dash) in normal and AD mice treated with **RPS1** became more visible. Along the cerebral blood vessels, the cerebral cortex region of AD mice showed strong PA signals, whereas the same region of normal mice displayed dim photoacoustic signals. The green–red color of PA images represents a higher Cu^{2+} concentration in the cortex regions (blue arrows). This phenomenon was more obvious in 3D PA imaging (Supporting Information, Movies 2_3D and 3_3D). To determine the biodistribution of **RPS1** in living mice, ex vivo PA images of major organs were acquired. As shown in Figure S26 in the Supporting Information, compared with control group, PA signals of the liver, kidney, and brain of the **RPS1**-treated group were significantly enhanced after intravenous injection of probe for 1.5 h, indicating that the probe was mainly metabolized by liver and kidney and enriched in the brain. After PA imaging, the brains were sliced and stained using Congo red and H&E for observation. Notably, Congo-red staining of AD brain slices showed plaques deposition in the hippocampus region. Shrunken cell nuclei were also found in this region using H&E staining of AD brain slices. These are neurodegenerative characters of AD (Figure 2c). Thus, this result provided visual evidence that **RPS1** could effectively cross the BBB and detect Cu^{2+} in the whole brains of normal and AD mice by the PA technique. Furthermore, the study also verified the higher level of Cu^{2+} in AD mice compared to normal mice by PA imaging for the first time.

Different from conventional PA probes with extended π-conjugation, **RPS** probes with low molecular weight can specifically chelate Cu^{2+} to form radicals with a turn-on PA response in the NIR region. Introducing the electron-donating group *N,N*-dimethylaniline was found to dramatically improve the stability of the probe–Cu radical and enhance the NIR PA intensity. Owing to the low molecular weight and amphiphilic structure, **RPS1** could effectively cross the BBB and achieve the visualization of Cu^{2+} in the whole brain of AD mice by PA imaging. This work provides a new design of PA probes and broadens the applications of PA-based sensing in the brain. We anticipate that this type of small-molecule probe will find a potential application in AD diagnosis, drug screening, and treatment evaluation.
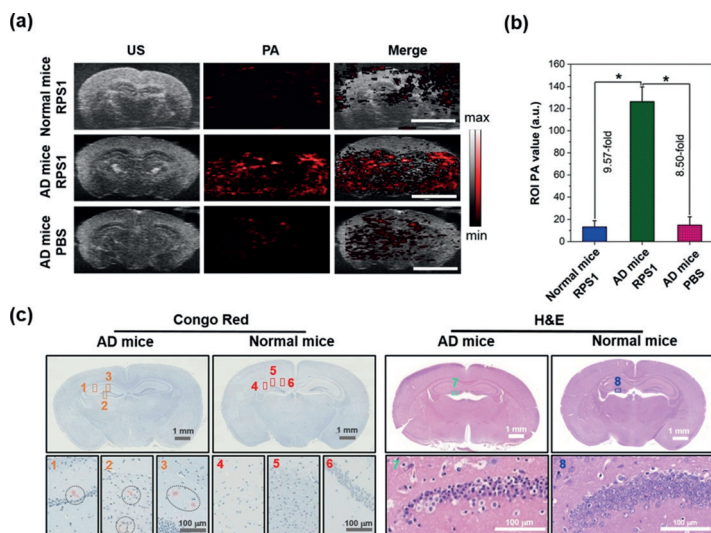

Figure 2. a) Representative PA images of from the brain of normal and AD mice after 1.5 h of intravenous injection of **RPS1** and PBS. The scale bar represents 5 mm. The scan wavelength of the laser was 750 nm at 10 mJ cm^{-2}. b) The PA intensity of normal and AD mice from ROI areas. Data presented as mean ± SD, *$p < 0.05$. c) Histological staining of the brain slices in the hippocampus region from mouse brains using Congo red and H&E.

Conflict of interest

The authors declare no conflict of interest.

[1] a) L. Zeng, E. W. Miller, A. Pralle, E. Y. Isacoff, C. J. Chang, *J. Am. Chem. Soc.* **2006**, *128*, 10–11; b) T. Hirayama, G. C. Van de Bittner, L. W. Gray, S. Lutsenko, C. J. Chang, *Proc. Natl. Acad. Sci. USA* **2012**, *109*, 2228–2233.

[2] K. P. Kepp, *Chem. Rev.* **2012**, *112*, 5193–5239.

[3] a) G. Multhaup, A. Schlicksupp, L. Hesse, D. Beher, T. Ruppert, C. L. Masters, K. Beyreuther, *Science* **1996**, *271*, 1406–1409; b) K. J. Barnham, C. L. Masters, A. I. Bush, *Nat. Rev. Drug Discovery* **2004**, *3*, 205–214; c) A. Rauk, *Chem. Soc. Rev.* **2009**, *38*, 2698–2715.

[4] a) J. A. Cotruvo, Jr., A. T. Aron, K. M. Ramos-Torres, C. J. Chang, *Chem. Soc. Rev.* **2015**, *44*, 4400–4414; b) E. L. Que, D. W. Domaille, C. J. Chang, *Chem. Rev.* **2008**, *108*, 1517–1549.

[5] a) G. Sivaraman, M. Iniya, T. Anand, N. G. Kotla, O. Sunnapu, S. Singaravadivel, A. Gulyani, D. Chellappa, *Coord. Chem. Rev.* **2018**, *357*, 50–104; b) O. Veiseh, C. Sun, C. Fang, N. Bhattarai, J. Gunn, F. Kievit, K. Du, B. Pullar, D. Lee, R. G. Ellenbogen, J. Olson, M. Zhang, *Cancer Res.* **2009**, *69*, 6200–6207; c) Y. S. Zhang, J. Yao, *Trends Biotechnol.* **2018**, *36*, 403–414; d) T. Branch, P. Girvan, M. Barahona, L. Ying, *Angew. Chem. Int. Ed.* **2015**, *54*, 1227–1230; *Angew. Chem.* **2015**, *127*, 1243–1246.

[6] a) C. Kim, C. Favazza, L. V. Wang, *Chem. Rev.* **2010**, *110*, 2756–2782; b) L. V. Wang, J. Yao, *Nat. Methods* **2016**, *13*, 627–638.

[7] a) S. Mallidi, G. P. Luke, S. Emelianov, *Trends Biotechnol.* **2011**, *29*, 213–221; b) E. I. Galanzha, E. V. Shashkov, T. Kelly, J. W. Kim, L. Yang, V. P. Zharov, *Nat. Nanotechnol.* **2009**, *4*, 855–860; c) X. Wang, D. L. Chamberland, D. A. Jamadar, *Opt. Lett.* **2007**, *32*, 3002–3004; d) Y. Wang, X. Hu, J. Weng, J. Li, Q. Fan, Y. Zhang, D. Ye, *Angew. Chem. Int. Ed.* **2019**, *58*, 4886–4890; *Angew. Chem.* **2019**, *131*, 4940–4944; e) Y. Jiang, P. K. Upputuri, C. Xie, Z. Zeng, A. Sharma, X. Zhen, J. Li, J. Huang, M. Pramanik, K. Pu, *Adv. Mater.* **2019**, *31*, 1808166; f) X. Zhen, J. Zhang, J. Huang, C. Xie, Q. Miao, K. Pu, *Angew. Chem. Int. Ed.* **2018**, *57*, 7804–7808; *Angew. Chem.* **2018**, *130*, 7930–7934.

[8] a) C. J. Reinhardt, E. Y. Zhou, M. D. Jorgensen, G. Partipilo, J. Chan, *J. Am. Chem. Soc.* **2018**, *140*, 1011–1018; b) S. C. Wang, Z. Li, Y. B. Liu, G. Feng, J. Zheng, Z. Yuan, X. J. Zhang, *Sens. Actuators B* **2018**, *267*, 403–411; c) J. Zhang, X. Zhen, P. K. Upputuri, M. Pramanik, P. Chen, K. Pu, *Adv. Mater.* **2017**, *29*, 1604764; d) B. Shi, X. Gu, Q. Fei, C. Zhao, *Chem. Sci.* **2017**, *8*, 2150–2155; e) Q. Chen, C. Liang, X. Sun, J. Chen, Z. Yang, H. Zhao, L. Feng, Z. Liu, *Proc. Natl. Acad. Sci. USA* **2017**, *114*, 5343–5348; f) K. Pu, A. J. Shuhendler, J. V. Jokerst, J. Mei, S. S. Gambhir, Z. Bao, J. Rao, *Nat. Nanotechnol.* **2014**, *9*, 233–239; g) J. Zhang, X. Zhen, J. Zeng, K. Pu, *Anal. Chem.* **2018**, *90*, 9301–9307; h) E. Y. Zhou, H. J. Knox, C. J. Reinhardt, G. Partipilo, M. J. Nilges, J. Chan, *J. Am. Chem. Soc.* **2018**, *140*, 11686–11697.

[9] a) H. J. Knox, J. Hedhli, T. W. Kim, K. Khalili, L. W. Dobrucki, J. Chan, *Nat. Commun.* **2017**, *8*, 1794; b) H. J. Knox, T. W. Kim, Z. Zhu, J. Chan, *ACS Chem. Biol.* **2018**, *13*, 1838–1843; c) S. Roberts, M. Seeger, Y. Jiang, A. Mishra, F. Sigmund, A. Stelzl, A. Lauri, P. Symvoulidis, H. Rolbieski, M. Preller, X. L. Dean-Ben, D. Razansky, T. Orschmann, S. C. Desbordes, P. Vetschera, T. Bach, V. Ntziachristos, G. G. Westmeyer, *J. Am. Chem. Soc.* **2018**, *140*, 2718–2721; d) H. Li, P. Zhang, L. P. Smaga, R. A. Hoffman, J. Chan, *J. Am. Chem. Soc.* **2015**, *137*, 15628–15631; e) Y. Liu, S. Wang, Y. Ma, J. Lin, H. Y. Wang, Y. Gu, X. Chen, P. Huang, *Adv. Mater.* **2017**, *29*, 1606129.

[10] a) L. Zeng, G. Ma, H. Xu, J. Mu, F. Li, X. Gao, Z. Deng, J. Qu, P. Huang, J. Lin, *Small* **2019**, *15*, 1803866; b) N. W. Pino, J. Davis III, Z. Yu, J. Chan, *J. Am. Chem. Soc.* **2017**, *139*, 18476–18479.

[11] a) H. J. Knox, J. Chan, *Acc. Chem. Res.* **2018**, *51*, 2897–2905; b) L. Zeng, G. Ma, J. Lin, P. Huang, *Small* **2018**, *14*, 1800782; c) S. Banala, S. Fokong, C. Brand, C. Andreou, B. Krautler, M. Rueping, F. Kiessling, *Chem. Sci.* **2017**, *8*, 6176–6181.

[12] a) R. C. Young, R. C. Mitchell, T. H. Brown, C. R. Ganellin, R. Griffiths, M. Jones, K. K. Rana, D. Saunders, I. R. Smith, N. E. Sore, et al., *J. Med. Chem.* **1988**, *31*, 656–671; b) K. Serdons, T. Verduyckt, D. Vanderghinste, P. Borghgraef, J. Cleynhens, F. Van Leuven, H. Kung, G. Bormans, A. Verbruggen, *Eur. J. Med. Chem.* **2009**, *44*, 1415–1426.

[13] M. W. Beck, J. S. Derrick, R. A. Kerr, S. B. Oh, W. J. Cho, S. J. Lee, Y. Ji, J. Han, Z. A. Tehrani, N. Suh, S. Kim, S. D. Larsen, K. S. Kim, J. Y. Lee, B. T. Ruotolo, M. H. Lim, *Nat. Commun.* **2016**, *7*, 13115.

[14] a) G. Buncic, Z. Xiao, S. C. Drew, J. M. White, A. G. Wedd, P. S. Donnelly, *Chem. Commun.* **2012**, *48*, 2570–2572; b) M. Bhadra, J. Y. C. Lee, R. E. Cowley, S. Kim, M. A. Siegler, E. I. Solomon, K. D. Karlin, *J. Am. Chem. Soc.* **2018**, *140*, 9042–9045; c) C. C. Chang, H. Yueh, C. T. Chen, *Org. Lett.* **2011**, *13*, 2702–2705.

[15] a) I. Fenoglio, M. Tomatis, D. Lison, J. Muller, A. Fonseca, J. B. Nagy, B. Fubini, *Free Radical Biol. Med.* **2006**, *40*, 1227–1233; b) W. K. Pogozelski, T. D. Tullius, *Chem. Rev.* **1998**, *98*, 1089–1108.

[16] Z. Sheng, B. Guo, D. Hu, S. Xu, W. Wu, W. H. Liew, K. Yao, J. Jiang, C. Liu, H. Zheng, B. Liu, *Adv. Mater.* **2018**, *30*, 1800766.

[17] D. Ni, J. Zhang, W. Bu, H. Xing, F. Han, Q. Xiao, Z. Yao, F. Chen, Q. He, J. Liu, S. Zhang, W. Fan, L. Zhou, W. Peng, J. Shi, *ACS Nano* **2014**, *8*, 1231–1242.

[18] a) M. Kaya, B. Ahishali, *Permeability Barrier*, Springer, Berlin, **2011**, pp. 369–382; b) K. H. Shim, K. H. Jeong, S. O. Bae, M. O. Kang, E. H. Maeng, C. S. Choi, Y. R. Kim, J. Hulme, E. K. Lee, M. K. Kim, S. S. An, *Int. J. Nanomed.* **2014**, *9 Suppl 2*, 225–233.

[19] Y. Yu, L. Zhang, C. Li, X. Sun, D. Tang, G. Shi, *Angew. Chem. Int. Ed.* **2014**, *53*, 12832–12835; *Angew. Chem.* **2014**, *126*, 13046–13049.